This document is downloaded from DR-NTU (https://dr.ntu.edu.sg)
Nanyang Technological University, Singapore.

Electrically controllable router of interlayer excitons

Liu, Yuanda; Dini, Kévin; Tan, Qinghai; Liew, Timothy Chi Hin; Novoselov, Kostya S.; Gao, Weibo

2020

Liu, Y., Dini, K., Tan, Q., Liew, T. C. H., Novoselov, K.S., & Gao, W. (2020). Electrically controllable router of interlayer excitons. Science Advances, 6(41), eaba1830-. doi:10.1126/sciadv.aba1830

https://hdl.handle.net/10356/145385

https://doi.org/10.1126/sciadv.aba1830

© 2020 The Authors, some rights reserved; exclusive licensee American Association for the Advancement of Science. No claim to original U.S. Government Works. Distributed under a Creative Commons Attribution NonCommercial License 4.0 (CC BY-NC).

Downloaded on 27 Aug 2022 18:30:42 SGT

CONDENSED MATTER PHYSICS

Electrically controllable router of interlayer excitons

Yuanda Liu[1,2], Kévin Dini[1], Qinghai Tan[1], Timothy Liew[1], Kostya S. Novoselov[3]*, Weibo Gao[1,2]*

Copyright © 2020 The Authors, some rights reserved; exclusive licensee American Association for the Advancement of Science. No claim to original U.S. Government Works. Distributed under a Creative Commons Attribution NonCommercial License 4.0 (CC BY-NC).

Optoelectronic devices that allow rerouting, modulation, and detection of the optical signals would be extremely beneficial for telecommunication technology. One of the most promising platforms for these devices is excitonic devices, as they offer very efficient coupling to light. Of especial importance are those based on indirect excitons because of their long lifetime. Here, we demonstrate excitonic transistor and router based on bilayer WSe_2. Because of their strong dipole moment, excitons in bilayer WSe_2 can be controlled by transverse electric field. At the same time, unlike indirect excitons in artificially stacked heterostructures based on transition metal dichalcogenides, naturally stacked bilayers are much simpler in fabrication.

INTRODUCTION

Increasing demand for faster telecommunication technologies calls for the shift of signal processing from electronic to optical domain. A very promising opportunity in this area is provided by excitonic devices (*1*–*5*). These devices convert light into excitons, manipulate excitons by means of electric or magnetic fields, and convert excitons back to light. Of particular importance are devices based on indirect excitons, which offer much longer (up to two orders of magnitude) lifetime in comparison with the direct excitons (*6*–*8*).

Originally designed on the type II quantum wells in GaAs/AlGaAs heterostructures, these devices offered extended lifetime of indirect excitons (*3*–*5*, *9*). With the advent of two-dimensional (2D) materials and, especially, transition metal dichalcogenides (TMDC), it became possible to form new types of type II quantum wells by combining TMDCs of different chemical compositions (*10*–*18*). These materials are potentially more promising for optoelectronic devices because of larger exciton binding energy (hundreds of millielectronvolts), which should enable them to be operational at elevated temperatures. It has been demonstrated that the optoelectronic devices based on stacked monolayers of TMDC can be operational at room temperatures (*1*, *19*). Moreover, the III-V thin films are generally achieved by epitaxial growth at high temperature using molecular beam epitaxy or metalorganic chemical vapor deposition. These apparatuses are very expensive because of the sophisticated reactors and high vacuum systems. The strain induced by the lattice mismatch at the interface results in high concentration of defects. Differently, the 2D material heterostructures are combined by van der Waals force; therefore, their single-crystal behavior is well inhibited. However, stacking of TMDCs to form van der Waals heterostructures is a tedious process, which often results in contamination of the interface and leads to nonradiative losses. The difference between the intrinsic bilayer sample and the layer-by-layer fabricated heterostructure can actually be observed by microscopy. The former one has flat and clean surface, while the fabricated MoS_2/WSe_2 heterostructure often has bubbles and rough surface. Recent experiments show that the Moire pattern formed in stacking heterostructures can impede exciton diffusion (*20*, *21*). Furthermore, the crystallographic directions of the stacked crystals have to be aligned to minimize momentum mismatch between electron and hole in such indirect exciton, which presents a substantial technological problem should these devices go to applications (*22*–*27*).

Here, we propose to use naturally occurring 2H stacked bilayer of WSe_2 to produce indirect excitons. Electrons and holes get separated to the different layers, forming spatially indirect excitons. Unlike mechanically stacked van der Waals heterostructures based on different layers of TMDC, our naturally stacked bilayer WSe_2 does not have any contaminants between the layers, thus providing a very high quality of heterostructures, a higher photoluminescence (PL) emission efficiency, and a very long lifetime of indirect excitons. The potential energy and binding energy can be controlled by the transverse electric field, which allows us to manipulate these indirect excitons remotely and demonstrate transistor and router behavior.

RESULTS

Our samples have been produced from 2H bounded bilayer WSe_2 by stacking it between two thick (approximately 20 nm) hexagonal boron nitride (hBN) crystals (see Materials and Methods for the details of the sample preparation). The whole stack was transferred on the Si/SiO_2 substrate with prepatterned gold electrodes (the particular shape of the electrodes depends on the particular experiment). A global graphene gate has been transferred on top of the whole stack. All measurements presented in this work were performed with two devices. Device 1 has bottom electrodes shaped as a series of parallel stripes (Figs. 1 and 2). The geometry of device 2 is designed to be a three-beam star (Figs. 3 and 4).

We first measured the PL spectra and spatial emission to characterize device 1. Bilayer WSe_2 is an indirect band gap semiconductor due to the finite interlayer coupling. Its valence band maximum and conduction band minimum are located at the K(K′) and Q(Q′) points of the Brillouin zone, respectively. Therefore, the lowest-energy optical transitions in bilayer WSe_2 are indirect transitions between the K and Q valleys (*6*, *28*). We note here that the upper layer and bottom layer of bilayer WSe_2 have a different surrounding environment (with hBN and graphene or hBN and gold electrode). This will shift the binding energy of excitons in the upper layer and bottom layer (*29*) and therefore shift the conduction and valence band to form the type II band alignment. Holes will be in the bottom layer and electrons will be in the upper layer to form the interlayer excitons (IXs). Figure 1A shows that the interlayer exciton emission has a peak wavelength at ~784 nm, which agrees with K-Q (K′-Q′) transitions. The fixed orientation of the exciton dipole direction also agrees with experiment

[1]Division of Physics and Applied Physics, School of Physical and Mathematical Sciences, Nanyang Technological University, Singapore 637371, Singapore. [2]The Photonics Institute and Centre for Disruptive Photonic Technologies, Nanyang Technological University, Singapore. [3]Department of Material Science and Engineering, National University of Singapore, 117575, Singapore.
*Corresponding author. Email: kostya@nus.edu.sg (K.S.N); wbgao@ntu.edu.sg (W.G.)

Downloaded from http://advances.sciencemag.org/ on December 17, 2020

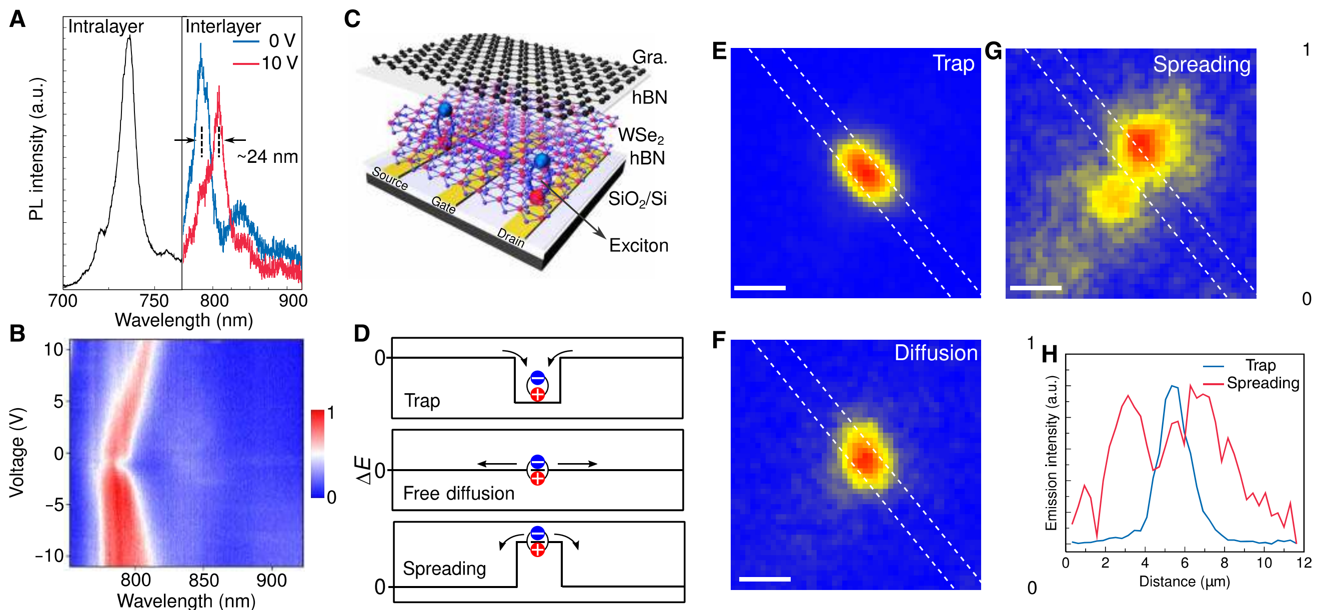

Fig. 1. Control 2D potential energy of interlayer excitons by electrical field. (**A**) PL of WSe_2 bilayer. The emission centering at ~736 and ~784 nm are ascribed to the intralayer excitons and interlayer excitons transition, respectively. PL spectra of interlayer exciton for gate voltage of 0 and 10 V, showing that the peak position redshifts by ~24 nm. Sample temperature is 10 K. a.u., arbitrary units. (**B**) Contour plot of the interlayer exciton emission intensity as a function of the applied gate voltage and wavelength. The excitation power is 30 μW operated at 532 nm. (**C**) Schematic structural diagram of one excitonic transistor. (**D**) Schematic of exciton energy offset for exciton dynamic regimes of trap, free diffusion, and spreading when applying negative (top), zero (middle), and positive (bottom) gate voltages, respectively. (**E** to **G**) Real-space emission intensity map for exciton trap, diffusion, and spreading, corresponding to gate voltage $V_G = -9$, 0, and 11 V, respectively. The white dashed lines indicate the bottom electrode edges. Scale bars, 2 μm. (**H**) Emission intensity profiles across the electrode extracted from the real-space emission intensity maps. The excitation spot was focused on the center of the electrode. The excitation power is ~200 nW operated at 532 nm.

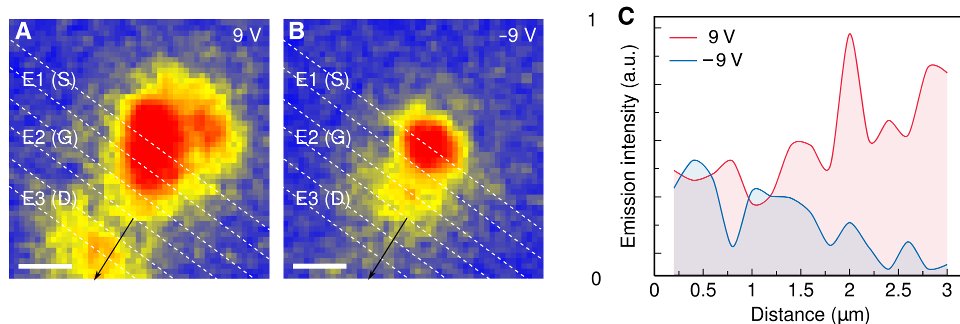

Fig. 2. Exciton transistor operations. Real-space emission intensity map for exciton ON and OFF operation, corresponding to voltage applied to electrode 2 [E2 (G)] $V_G = 9$ V (**A**), −9 V (**B**), respectively. The voltage applied to electrode 1 [E1 (S)] and electrode 3 [E3 (D)] is 4 and 0 V, respectively. The white dashed lines indicate the bottom electrode edges. Scale bars, 2 μm. (**C**) Emission intensity profiles along the solid black arrows in (A) and (B). The excitation power is ~600 nW operated at 532 nm. Both $V_G = 0$ and 9 V can be seen as ON state, which is in stark difference with $V_G = -9$ V (OFF state).

demonstrated below. The wavelength does not overlap with the intralayer exciton emission (~736 nm) (*6*, *30*). This permits us to remove the intralayer exciton emission using optical long-pass filters. We have compared the PL emission intensity for intrinsic WSe_2 bilayer and the samples by stacking two different monolayer WSe_2. Our experiments show that intrinsic bilayer has an interlayer exciton emission intensity around one order larger than those of stacked bilayers (fig. S2).

We characterize the exciton wavelength and lifetime, as shown in Fig. 1B and fig. S3. Electric field (Fig. 1B) shows continuous wide tunability of exciton wavelength, which is actually a combined effect of binding energy tuning, Coulomb scattering, and screening of the Coulomb interaction, as well as change of repulsive interaction with electric field (*31*). Time-resolved PL measurements (fig. S4) reveal a lifetime well in the nanosecond time range, representing two orders of magnitude improvement over that of intralayer excitons, allowing formation of a long-lived 2D exciton gas (*6*). Within this lifetime, IXs travel over a long distance larger than the device dimensions. Electric-exciton interaction controls 2D potential for IXs in atomically thin homogeneous material, as schematically illustrated in Fig. 1C.

We demonstrated 2D potential energy controllability of interlayer excitons by an out-of-plane electric field. An interlayer exciton has

Downloaded from http://advances.sciencemag.org/ on December 17, 2020

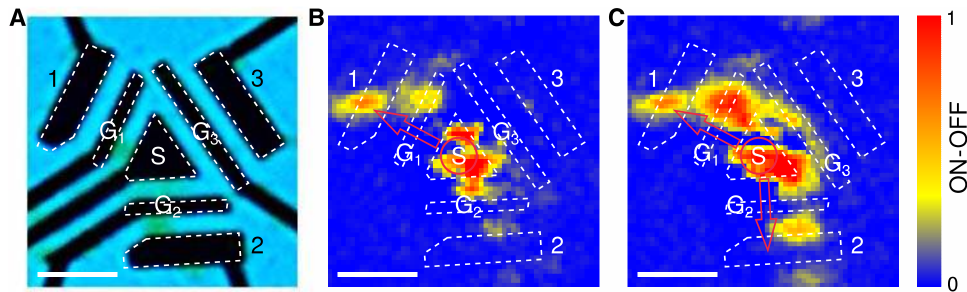

Fig. 3. Unidirectional movement for excitonic transistor operation. (**A**) Optical image of the device. The black areas are the bottom electrodes. (**B**) Real-space emission intensity map when one transistor is in ON state. The $V_S = 0$ V and $V_{D1} = -1$ V create a potential energy offset, and the perturbation in gate voltage $\Delta V_{G1} = 20$ V. To improve the contrast of the image, the image shows the normalized PL intensity difference between ON and OFF state when $V_{G1,ON} = 10$ V and $V_{G1,OFF} = -10$ V. No voltages were applied on transistors 2 and 3. (**C**) Real-space emission intensity map when switching on the second transistor. $V_S = 0$ V, $V_{D2} = -1$ V, $V_{G2,ON} = 10$ V, and $V_{G2,OFF} = -10$ V. Voltages applied on transistor 1 are the same as those in (B). No voltages were applied on transistor 3. The white dashed lines indicate the bottom electrode edges. The excitation spot was focused on the center of the triangle electrode. The solid red arrows are a guide to the eye. The excitation power is ~100 μW operated at 730 nm. Scale bars, 5 μm.

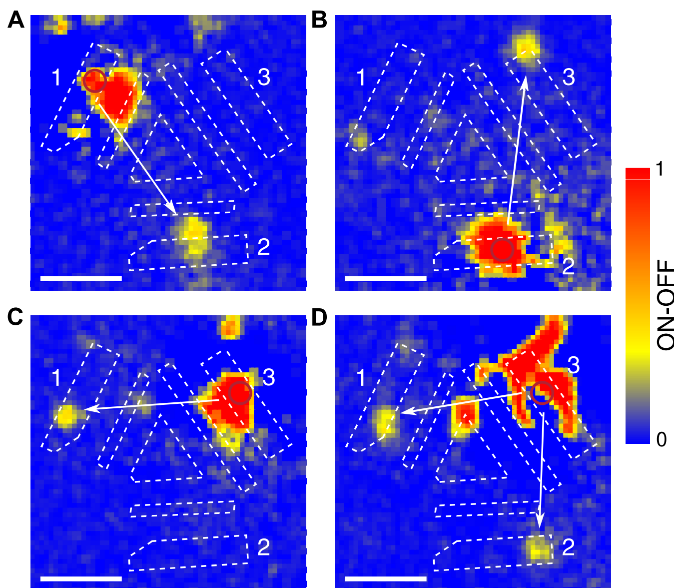

Fig. 4. Point-to-point movement for excitonic router operation. The exciton signal routing can be achieved by directly applying electric gate voltage on ports 1, 2, and 3. All gate voltages are set to zero. (**A**) Exciton propagation from port 1 to port 2; $V_1 = 0$ V, $V_3 = 3$ V, $V_{2,ON} = -3$ V, and $V_{2,OFF} = 3$ V. (**B**) Exciton propagation from port 2 to port 3; $V_1 = 8$ V, $V_2 = 0$ V, $V_{3,ON} = -1$ V, and $V_{3,OFF} = 10$ V. (**C**) Exciton propagation from port 3 to port 1; $V_2 = 4$ V, $V_3 = 0$ V, $V_{1,ON} = -0.5$ V, and $V_{1,OFF} = 6$ V. (**D**) Excitons propagation from port 3 to both port 1 and port 2; $V_3 = 0$ V, $V_{1,ON} = 0$ V, $V_{1,OFF} = 8$ V, $V_{2,ON} = 0$ V, and $V_{2,OFF} = 8$ V. To improve the contrast of the images, the images show the normalized PL intensity difference between ON and OFF state. The solid white arrows parallel to the excitons propagation direction are drawn as a guide to the eye. The red circles show the laser excitation spot. The excitation power is ~200 μW operated at 730 nm. Scale bars, 5 μm.

a dipole moment p with an out-of-plane (z) direction due to the separation and confinement of composed electron and hole in spatially separated layers [layer separation is ~0.78 nm for WSe_2 bilayer, as measured by atomic force microscopy (AFM); fig. S4]. Therefore, the application of an out-of-plane electric field Fz leads to an exciton energy shift (*2*, *32*, *33*) of $\Delta E = ed$Fz, where ed is the built-in dipole moment of IXs, and d is the electron-hole separation distance in the exciton. With a fixed exciton dipole direction, the electric field can therefore create lower or higher energy potential along the electrode and therefore drives the confinement and spread of excitons.

The excitons will be driven toward regions of lower energy in the 2D potential energy surface. We apply voltage to one of the bottom electrodes, while the top graphene is grounded. Therefore, a negative voltage creates a downward vertical electric field that lowers the exciton electrostatic potential by $\Delta E = ed$Fz (top panel in Fig. 1D), yielding a potential well overlapping the area of the bottom electrode. The experimental measurement of the exciton spatial movement is performed using the setup shown in fig. S5. The real-space emission map (Fig. 1E) shows unambiguous exciton confinement and diffusion along the electrode with an elongated shape.

On the contrary, when the exciton potential is increased by a positive voltage (bottom panel in Fig. 1D), the excitons are spreading away from the antichannel. The real-space emission map for the spreading is displayed in Fig. 1G. The emission trace extends in a direction perpendicular to the electrode rather than a circular cylinder around the laser spot (free diffusion shown in Fig. 1F), indicative of realization of a long-range excitonic unidirectional movement driven electrically. Note that the position of the emission maximum shifts away from the illumination point to the side of the electrode, benefitting from the long lifetime of IXs. Figure 1H plots the emission intensity profiles along the flux trace extracted from Fig. 1 (E and G), showing the transition from trap regime to the spreading regime by modulating the gate voltage. An emission intensity valley at the excitation spot implies the highly tunable potential. Figure S6 exhibits the real-space emission map of excitons for gate voltage $V_G = -14$ to 14 V at a step of 1 V. For device 2, when excitation is on the gate electrode and gate voltage applied to that electrode, similar confinement and spreading are observed and are shown in fig. S7 for PL emission pattern difference between $V_G = 10$ and -10 V. The intralayer exciton binding energy in monolayer WSe_2 is determined to be hundreds of millielectronvolts (*34*), which is two orders higher than that in GaAs (4.2 ± 0.3 meV) (*35*). The generation of robust excitons renders the exciton excited states and the exciton drifting behavior observable at elevated temperatures as high as 250 K (fig. S9), which unambiguously surpasses that of conventional III-V semiconductors.

The exciton flux can be controlled by an electric field in the prorogation midway, as exhibited in Fig. 2. The laser light was illustrated on the source (S) electrode area. The generated excitons propagate away from the excitation site. When a negative voltage V_G was applied to the G electrode, an exciton potential well is created in the gate electrode area, resulting in the termination of the exciton flux. Only noise signal can be detected on the drain (D) electrode, as shown in

Downloaded from http://advances.sciencemag.org/ on December 17, 2020

Fig. 2A. This agrees with the exciton transistor, as demonstrated with GaAs double quantum wells (*4*). A positive voltage of V_G applied to the G electrode can separate emission area on the source electrode and drain electrode but will not fully block the diffusion of exciton flux (Fig. 2B). We can therefore define V_G = 9 V as the ON state and V_G = −9 V as the OFF state for the intensity on the drain electrode. Figure S8 shows the real-space emission map of excitons for G voltage V_G = −9 to 9 V at a step of 2 V. We extracted the cross-sectional profiles parallel and perpendicular to the IXs transporting trace. Figure 3C plots the emission intensity along exciton flux (black arrows in Fig. 2, A and B). The calculated ON/OFF ratio reaches ~6 (fig. S9), limited by the noise level of the detector. The distance between the centerlines of the source and drain electrodes is ~4 μm. ON/OFF ratio is around unity outside the drain electrode, increases to ~6 on the drain electrode area, indicative of the functionality and the accuracy of our exciton transistor.

Unidirectional excitonic transistor operation

Next, we demonstrate excitonic switching on the basis of the unidirectional movement of excitons. An excitonic circuit composed of three exciton transistors was fabricated (see Materials and Methods for detailed fabrication process). Figure 3A shows the optical image of the circuit. Excitonic transistor is designed to be a device with three terminals, including source, gate, and drain, as schematically shown in Fig. 1C. It operates like an electric field-effect transistor (*36*–*38*), which works by modulating the electrical charge carrier density and, hence, electrical resistance of a thin semiconducting channel through the application of an electric field using gate. The exciton intensity difference drives the IXs generated under excitation to move from the source toward the drain. Application of a gate voltage electrostatically modulates the prorogation distance and concentration. A negative voltage traps the IXs in the region of the gate, thereby lessening the IXs concentration propagating to drain. In our design, three transistors have a common electrode, the triangle electrode, as shown in Fig. 3A.

We examine the net effects of the gate voltage on the IXs population distribution. Figure 3 (B and C) present real-space emission maps when illustrating at the center of triangle electrode. To this end, the net increment of the emission intensity is the difference of PL emission when transistor is in ON state (gate electrode, 10 V) and OFF state (−10 V). This also avoids the noise of the background induced by the measuring system. The emission image for one transistor in ON state is shown in Fig. 3A. The V_S = 0 V and V_D = −1 V create a potential energy offset, and the perturbation in gate voltage ΔV_G = 20 V. In the device, the distance between the source and drain is 4 μm. At the same time, the other two transistors are kept inactive. The star geometry of the circuit allows star switching. Figure 3C shows that transistor 2 is also switched on. The IXs flux is routed simultaneously on two paths with an angle of 120°.

Excitonic router operation

We further reconfigure the same circuit to demonstrate a point-to-point movement to implement device functionality of exciton circulation. We consider the three outer electrodes as the three ports of a router, which are denoted by ports 1, 2, and 3 in Fig. 4, respectively. First, the excitation laser spot is focused on port 1. Potential energy difference is created by the application of voltages on drain electrode port 1 (0 V) and port 2 (−3 V), while applying a high voltage (3 V) on port 3. Such a regime allows excitons generated at port 1 to only be transmitted to port 2. Figure 4 (B and C) shows the exciton propagation from port 2 to only port 3 and, likewise, from port 3 to only port 1. Figure 4D displays that the excitons move from port 3 to port 1 and port 2 simultaneously. The excitons transmit either to one port or two ports depending on the voltage application. Therefore, the router is programmable, and its operation direction is defined by the electric voltages applied on each port. The slight emission on the corner of port 1 in Fig. 4B is caused by a nonideal device. The essential ingredients of our excitonic router are the all-optical input-output signal processing, the miniaturization of device dimensions, and the flexibility of low-voltage electrical driving scheme.

DISCUSSION

In summary, our experiments demonstrate electrical controllability of exciton dynamics in atomically thin homogeneous materials, presenting exciton propagation in a controlled direction. This enables a conceptual design of miniaturized on-chip all-optical devices, the excitonic switching, and the excitonic routing in an integrated circuit. We envision that this proof-of-concept device may pave a promising way for developing practical exciton-related applications and inject new vitality into research in this bosonic particle.

MATERIALS AND METHODS

Sample fabrication

The exciton devices are composed of the bottom electrodes, two hBN gate dielectric layers, a WSe_2 bilayer, and a graphene homogeneous top gate. The bottom electrodes were patterned using standard electron beam lithography followed by sputtering of Au (~10 nm) onto 285-nm-thick SiO_2/Si substrate. Intrinsic silicon was adopted to considerably decrease the background emission intensity. WSe_2 bilayer, hBN, and graphene were mechanically exfoliated from bulk single crystals and were subsequently stacked by means of dry transfer onto the bottom electrodes (*39*). The layer number of WSe_2 was identified by a combination of optical contrast, PL spectroscopy, and AFM. The hBN is relatively thick with ~20-nm thickness. As a dielectric insulator layer, it separates the graphite and WSe_2, preventing the quenching effect. A second step of electron beam lithography was performed to define the top gate metallic contacts (Ti/Au = 3/60 nm) followed by electron-beam evaporation and liftoff.

Optical characterization

Device was mounted on the cold head of a closed-cycle helium cryostat with variable temperature (5 K < T < 350 K). Optical measurement was performed with a customized optical setup (see fig. S5 for more details). We excited the sample with the above-bandgap continuous-wave lasers focused to a ~1-μm spot on the surface of the sample using a 50× long–working distance microscope objective lens (numerical aperture = 0.65). The scattered PL signal was collected vertically by the same objective. Laser spot was positioned using either a piezoelectric nanopositioner or a galvo mirror pair. To measure the spatial emission maps, the PL signal was descanned by another galvo mirror pair and detected by a single-photon detector. Filters were used in all experiments to prevent pump light from reaching any detectors or cameras. The pumping power was adjusted using a neutral density filter. The electric voltage was applied using a Keithley 4200-SCS semiconductor parameter analyzer and a Keithley 2450 SourceMeter.

Downloaded from http://advances.sciencemag.org/ on December 17, 2020

SUPPLEMENTARY MATERIALS

Supplementary material for this article is available at http://advances.sciencemag.org/cgi/content/full/6/41/eaba1830/DC1

REFERENCES AND NOTES

1. D. Unuchek, A. Ciarrocchi, A. Avsar, K. Watanabe, T. Taniguchi, A. Kis, Room-temperature electrical control of exciton flux in a van der Waals heterostructure. *Nature* **560**, 340–344 (2018).
2. P. Andreakou, S. V. Poltavtsev, J. R. Leonard, E. V. Calman, M. Remeika, Y. Y. Kuznetsova, L. V. Butov, J. Wilkes, M. Hanson, A. C. Gossard, Optically controlled excitonic transistor. *Appl. Phys. Lett.* **104**, 091101 (2014).
3. Y. Y. Kuznetsova, M. Remeika, A. A. High, A. T. Hammack, L. V. Butov, M. Hanson, A. C. Gossard, All-optical excitonic transistor. *Opt. Lett.* **35**, 1587–1589 (2010).
4. G. Grosso, J. Graves, A. T. Hammack, A. A. High, L. V. Butov, M. Hanson, A. C. Gossard, Excitonic switches operating at around 100 K. *Nat. Photonics* **3**, 577–580 (2009).
5. A. A. High, E. E. Novitskaya, L. V. Butov, M. Hanson, A. C. Gossard, Control of exciton fluxes in an excitonic integrated circuit. *Science* **321**, 229–231 (2008).
6. Z. Wang, Y.-H. Chiu, K. Honz, K. F. Mak, J. Shan, Electrical tuning of interlayer exciton gases in WSe_2 bilayers. *Nano Lett.* **18**, 137–143 (2017).
7. B. Miller, A. Steinhoff, B. Pano, J. Klein, F. Jahnke, A. Holleitner, U. Wurstbauer, Long-lived direct and indirect interlayer excitons in van der Waals heterostructures. *Nano Lett.* **17**, 5229–5237 (2017).
8. P. Rivera, J. R. Schaibley, A. M. Jones, J. S. Ross, S. Wu, G. Aivazian, P. Klement, K. Seyler, G. Clark, N. J. Ghimire, J. Yan, D. G. Mandrus, W. Yao, X. Xu, Observation of long-lived interlayer excitons in monolayer $MoSe_2$-WSe_2 heterostructures. *Nat. Commun.* **6**, 6242 (2015).
9. A. A. High, A. T. Hammack, L. V. Butov, M. Hanson, A. C. Gossard, Exciton optoelectronic transistor. *Opt. Lett.* **32**, 2466–2468 (2007).
10. A. Ciarrocchi, D. Unuchek, A. Avsar, K. Watanabe, T. Taniguchi, A. Kis, Polarization switching and electrical control of interlayer excitons in two-dimensional van der Waals heterostructures. *Nat. Photonics* **13**, 131–136 (2019).
11. E. M. Alexeev, D. A. Ruiz-Tijerina, M. Danovich, M. J. Hamer, D. J. Terry, P. K. Nayak, S. Ahn, S. Pak, J. Lee, J. I. Sohn, M. R. Molas, M. Koperski, K. Watanabe, T. Taniguchi, K. S. Novoselov, R. V. Gorbachev, H. S. Shin, V. I. Fal'ko, A. I. Tartakovskii, Resonantly hybridized excitons in moiré superlattices in van der Waals heterostructures. *Nature* **567**, 81–86 (2019).
12. J. Kunstmann, F. Mooshammer, P. Nagler, A. Chaves, F. Stein, N. Paradiso, G. Plechinger, C. Strunk, C. Schüller, G. Seifert, D. R. Reichman, T. Korn, Momentum-space indirect interlayer excitons in transition-metal dichalcogenide van der Waals heterostructures. *Nat. Phys.* **14**, 801–805 (2018).
13. C. Jin, J. Kim, M. I. B. Utama, E. C. Regan, H. Kleemann, H. Cai, Y. Shen, M. J. Shinner, A. Sengupta, K. Watanabe, T. Taniguchi, S. Tongay, A. Zettl, F. Wang, Imaging of pure spin-valley diffusion current in WS2-WSe2 heterostructures. *Science* **360**, 893–896 (2018).
14. P. Nagler, M. V. Ballottin, A. A. Mitioglu, F. Mooshammer, N. Paradiso, C. Strunk, R. Huber, A. Chernikov, P. C. M. Christianen, C. Schüller, T. Korn, Giant magnetic splitting inducing near-unity valley polarization in van der Waals heterostructures. *Nat. Commun.* **8**, 1551 (2017).
15. J. Kim, C. Jin, B. Chen, H. Cai, T. Zhao, P. Lee, S. Kahn, K. Watanabe, T. Taniguchi, S. Tongay, M. F. Crommie, F. Wang, Observation of ultralong valley lifetime in WSe2/MoS2 heterostructures. *Sci. Adv.* **3**, e1700518 (2017).
16. M.-H. Chiu, C. Zhang, H.-W. Shiu, C.-P. Chuu, C.-H. Chen, C.-Y. S. Chang, C.-H. Chen, M.-Y. Chou, C.-K. Shih, L.-J. Li, Determination of band alignment in the single-layer MoS2/WSe2 heterojunction. *Nat. Commun.* **6**, 7666 (2015).
17. H. Fang, C. Battaglia, C. Carraro, S. Nemsak, B. Ozdol, J. S. Kang, H. A. Bechtel, S. B. Desai, F. Kronast, A. A. Unal, G. Conti, C. Conlon, G. K. Palsson, M. C. Martin, A. M. Minor, C. S. Fadley, E. Yablonovitch, R. Maboudian, A. Javey, Strong interlayer coupling in van der Waals heterostructures built from single-layer chalcogenides. *Proc. Natl. Acad. Sci. U.S.A.* **111**, 6198–6202 (2014).
18. M.-H. Chiu, M.-Y. Li, W. Zhang, W.-T. Hsu, W.-H. Chang, M. Terrones, H. Terrones, L.-J. Li, Spectroscopic signatures for interlayer coupling in MoS2–WSe2 van der Waals stacking. *ACS Nano* **8**, 9649–9656 (2014).
19. Y. Liu, H. Fang, A. Rasmita, Y. Zhou, J. Li, T. Yu, Q. Xiong, N. Zheludev, J. Liu, W. Gao, Room temperature nanocavity laser with interlayer excitons in 2D heterostructures. *Sci. Adv.* **5**, eaav4506 (2019).
20. L. Yuan, B. Zheng, J. Kunstmann, T. Brumme, A. B. Kuc, C. Ma, S. Deng, D. Blach, A. Pan, L. Huang, Twist-angle-dependent interlayer exciton diffusion in WS2–WSe2 heterobilayers. *Nat. Mater.* **19**, 617–623 (2020).
21. J. Choi, W.-T. Hsu, L.-S. Lu, L. Sun, H.-Y. Cheng, M.-H. Lee, J. Quan, K. Tran, C.-Y. Wang, M. Staab, K. Jones, T. Taniguchi, K. Watanabe, M.-W. Chu, S. Gwo, S. Kim, C.-K. Shih, X. Li, W.-H. Chang, Moir\'e potential impedes interlayer exciton diffusion in van der Waals heterostructures. arXiv:1912.11101 (2019).
22. P. K. Nayak, Y. Horbatenko, S. Ahn, G. Kim, J.-U. Lee, K. Y. Ma, A.-R. Jang, H. Lim, D. Kim, S. Ryu, H. Cheong, N. Park, H. S. Shin, Probing evolution of twist-angle-dependent interlayer excitons in MoSe2/WSe2 van der Waals heterostructures. *ACS Nano* **11**, 4041–4050 (2017).
23. E. M. Alexeev, A. Catanzaro, O. V. Skrypka, P. K. Nayak, S. Ahn, S. Pak, J. Lee, J. I. Sohn, K. S. Novoselov, H. S. Shin, A. I. Tartakovskii, E. M. Alexeev, A. Catanzaro, O. V. Skrypka, P. K. Nayak, S. Ahn, S. Pak, J. Lee, J. I. Sohn, K. S. Novoselov, H. S. Shin, A. I. Tartakovskii, Imaging of interlayer coupling in van der Waals heterostructures using a bright-field optical microscope. *Nano Lett.* **17**, 5342–5349 (2017).
24. H. Heo, J. H. Sung, S. Cha, B.-G. Jang, J.-Y. Kim, G. Jin, D. Lee, J.-H. Ahn, M.-J. Lee, J. H. Shim, H. Choi, M.-H. Jo, Interlayer orientation-dependent light absorption and emission in monolayer semiconductor stacks. *Nat. Commun.* **6**, 7372 (2015).
25. K. Tran, G. Moody, F. Wu, X. Lu, J. Choi, K. Kim, A. Rai, D. A. Sanchez, J. Quan, A. Singh, J. Embley, A. Zepeda, M. Campbell, T. Autry, T. Taniguchi, K. Watanabe, N. Lu, S. K. Banerjee, K. L. Silverman, S. Kim, E. Tutuc, L. Yang, A. H. MacDonald, X. Li, Evidence for moiré excitons in van der Waals heterostructures. *Nature* **567**, 71–75 (2019).
26. K. L. Seyler, P. Rivera, H. Yu, N. P. Wilson, E. L. Ray, D. G. Mandrus, J. Yan, W. Yao, X. Xu, Signatures of moiré-trapped valley excitons in MoSe2/WSe2 heterobilayers. *Nature* **567**, 66–70 (2019).
27. C. Jin, E. C. Regan, A. Yan, M. I. B. Utama, D. Wang, S. Zhao, Y. Qin, S. Yang, Z. Zheng, S. Shi, K. Watanabe, T. Taniguchi, S. Tongay, A. Zettl, F. Wang, Observation of moiré excitons in WSe2/WS2 heterostructure superlattices. *Nature* **567**, 76–80 (2019).
28. G.-B. Liu, D. Xiao, Y. Yao, X. Xu, W. Yao, Electronic structures and theoretical modelling of two-dimensional group-VIB transition metal dichalcogenides. *Chem. Soc. Rev.* **44**, 2643–2663 (2015).
29. A. Raja, A. Chaves, J. Yu, G. Arefe, H. M. Hill, A. F. Rigosi, T. C. Berkelbach, P. Nagler, C. Schüller, T. Korn, C. Nuckolls, J. Hone, L. E. Brus, T. F. Heinz, D. R. Reichman, A. Chernikov, Coulomb engineering of the bandgap and excitons in two-dimensional materials. *Nat. Commun.* **8**, 15251 (2017).
30. G. Wang, X. Marie, L. Bouet, M. Vidal, A. Balocchi, T. Amand, D. Lagarde, B. Urbaszek, Exciton dynamics in WSe_2 bilayers. *Appl. Phys. Lett.* **105**, 182105 (2014).
31. A. Chernikov, A. M. van der Zande, H. M. Hill, A. F. Rigosi, A. Velauthapillai, J. Hone, T. F. Heinz, Electrical tuning of exciton binding energies in monolayer WS2. *Phys. Rev. Lett.* **115**, 126802 (2015).
32. L. V. Butov, C. W. Lai, A. L. Ivanov, A. C. Gossard, D. S. Chemla, Towards Bose–Einstein condensation of excitons in potential traps. *Nature* **417**, 47–52 (2002).
33. D. A. B. Miller, D. S. Chemla, T. C. Damen, A. C. Gossard, W. Wiegmann, T. H. Wood, C. A. Burrus, Electric field dependence of optical absorption near the band gap of quantum-well structures. *Phys. Rev. B* **32**, 1043–1060 (1985).
34. K. He, N. Kumar, L. Zhao, Z. Wang, K. F. Mak, H. Zhao, J. Shan, Tightly bound excitons in monolayer WSe 2. *Phys. Rev. Lett.* **113**, 026803 (2014).
35. S. B. Nam, D. C. Reynolds, C. W. Litton, R. J. Almassy, T. C. Collins, C. M. Wolfe, Free-exciton energy spectrum in GaAs. *Phys. Rev. B* **13**, 761–767 (1976).
36. J. I.-J. Wang, Y. Yang, Y.-A. Chen, K. Watanabe, T. Taniguchi, H. O. H. Churchill, P. Jarillo-Herrero, Electronic transport of encapsulated graphene and WSe2 devices fabricated by pick-up of prepatterned hBN. *Nano Lett.* **15**, 1898–1903 (2015).
37. H. C. P. Movva, A. Rai, S. Kang, K. Kim, B. Fallahazad, T. Taniguchi, K. Watanabe, E. Tutuc, S. K. Banerjee, High-mobility holes in dual-gated WSe2 field-effect transistors. *ACS Nano* **9**, 10402–10410 (2015).
38. C. H. Ahn, J. M. Triscone, J. Mannhart, Electric field effect in correlated oxide systems. *Nature* **424**, 1015–1018 (2003).
39. L. Wang, I. Meric, P. Y. Huang, Q. Gao, Y. Gao, H. Tran, T. Taniguchi, K. Watanabe, L. M. Campos, D. A. Muller, J. Guo, P. Kim, J. Hone, K. L. Shepard, C. R. Dean, One-dimensional electrical contact to a two-dimensional material. *Science* **342**, 614–617 (2013).

Acknowledgments

Funding: This work is supported by the Singapore National Research Foundation through its Competitive Research Program (CRP Award No. NRF-CRP21-2018-0007), Singapore Ministry of Education [MOE2016-T2-2-077, MOE2016-T2-1-163, MOE2018-T3-1-002, and MOE2016-T3-1-006 (S)], and A*Star QTE programme. **Author contributions:** Y.L., K.D., Q.T., T.L., K.S.N., and W.G. contributed equally to the experimental work, analysis, and manuscript writing. **Competing interests:** The authors declare that they have no competing interests. **Data and materials availability:** All data needed to evaluate the conclusions in the paper are present in the paper and/or the Supplementary Materials. The data that support the plots within this paper and other findings of this study are available upon reasonable request.

Submitted 12 November 2019
Accepted 19 August 2020
Published 7 October 2020
10.1126/sciadv.aba1830

Citation: Y. Liu, K. Dini, Q. Tan, T. Liew, K. S. Novoselov, W. Gao, Electrically controllable router of interlayer excitons. *Sci. Adv.* **6**, eaba1830 (2020).

Downloaded from http://advances.sciencemag.org/ on December 17, 2020